FISEVIER

Contents lists available at ScienceDirect

Journal of Building Engineering

journal homepage: www.elsevier.com/locate/jobe





Wind loading on commercial roof edge metals: A full-scale experimental study

Ameyu B. Tolera ^{a,*}, Johnny Estephan ^a, Arindam Gan Chowdhury ^{a,b}, Ioannis Zisis ^{a,b}, Erica Sherman ^c, James Kirby ^c

- ^a Department of Civil and Environmental Engineering, Florida International University, Miami, FL, USA
- b Extreme Events Institute of International Hurricane Research Center, Florida International University, Miami, FL, USA
- ^c GAF Materials Corp, Parsippany, NJ, USA

ARTICLE INFO

Keywords: Edge metals Commercial roofs Wind loads Wind-induced vibrations Full-scale wind tunnel tests

ABSTRACT

Roof edge metal systems provide an effective interface between the roof of a building to its walls and are used to secure and protect the edge of the roof membrane. Previous studies show that damage involving roof systems mostly occurs because of their failure at perimeter edges under high winds. This study presents an effort to evaluate wind loads on these edge metal elements by conducting full-scale experiments at the NHERI Wall of Wind (WOW) Experimental Facility (EF) at Florida International University. In addition to full-scale aerodynamic and failure assessment test protocols, the experimental campaign, for the first time to the authors' knowledge, consisted of investigating the effect of wind-induced vibrations on these dynamically sensitive systems. Pressure measurements were conducted at different layers of the edge metals systems by considering the most common installation practices in the industry. The results showed that these roofing elements experience high suctions due to near-parallel wind flows and are susceptible to significant vibration even at low wind speeds, which is a phenomenon not captured in current static pull testing. Moreover, peak pressure coefficients were also observed to increase with wind speeds due to increased dynamic contributions which may amplify the aerodynamic loads by more than about 25%. Furthermore, utilization of edge metal configurations with a higher degree of flexibility was observed to possibly reduce suction on roofing components and appurtenances.

1. Introduction

Roof edge metals, used broadly on commercial and industrial roofs, function as an effective interface between the roof of a building to its walls. Typically, the edge metal system is comprised of a cleat fastened to the substrate and a coping or fascia that is frictionally attached to the cleat at its front lower ends and mechanically fastened to the roof or parapet at its back. Besides providing an aesthetical finish for the roof perimeters and protecting building components from water infiltration, they provide anchorage for roofing membranes and are the first line of defense during high-wind events. As they are situated in the most turbulent region of the roof surface where flow separation is prevalent, such systems are highly vulnerable to wind-induced damage. Results from the Roofing Industry Committee on Weather Issues (RICOWI) inspection of mechanically attached single-ply roofs in Florida after Hurricane Michael showed that 80% of the surveyed roofs sustained damage along their perimeter and 70% of them incurred edge metal failures [1]. Observations during past hurricanes also highlighted the dependence of the wind resistance of membrane roofing systems on their

^{*} Corresponding author.

E-mail address: atole066@fiu.edu (A.B. Tolera).

perimeter flashings. Disengagement or displacement of edge metals was deemed to be responsible for the failure of fully adhered roofs [2,3]. After the failure of edge metals, membranes were observed to have been torn or loosened, which in turn were also linked to interior damage as a result of water intrusion [3,4].

Previous studies investigated wind loads on and wind resistance of edge metal systems based on post-disaster reconnaissance surveys [4,5], field experiments [6,7], and field investigations [8,9]. [5] detailed the progressive failure mechanism particular to edge metal systems as observed after Hurricane Hugo. The study reported that most failures were due to the inadequate attachment of either the flashings themselves or the wood nailer. Similarly, four disengagement mechanisms were also reported by Ref. [8]: (1) fascia disengagement from the cleat, (2) cleat anchor failure, (3) fascia-cleat disengagement and cleat anchor pull-out, and (4) billowing membrane causing fascia anchor pull-out or damage to the fascia-membrane connection. Aerodynamic wind load evaluation studies have also shown that edge metal systems mostly experience suction even on the building's windward wall contrary to what is specified in building codes and standards, such as the American Society of Civil Engineers 7 and National Building Code of Canada (NBCC) [6-8]. Besides this external suction, it was reported that these systems are also subject to positive pressures that develop between the cleat and the substrate. Such pressures act in the direction of the external suction and push the system outwards causing anchor pull-out or fascia detachment from the cleat. [6] studied various edge metal configurations on the Wind Engineering Research Field Laboratory (WERFL) test building and reported mean pressure coefficients for the windward, leeward, parallel, and quartering wind directions. Later, [7] reported the mean, maximum, minimum, and standard deviation of pressure coefficients on the front and top faces and between the cleat and substrate of an edge metal system installed at the corner of the WERFL building. According to their study, minimum pressure coefficients ranging up to -1.9 and -3.7 were recorded on the front and top fascia faces, respectively. Recently, [8] also reported mean and peak pressure coefficients on three different roof edge metal configurations installed on parapets: anchor clip configuration (ACC), continuous cleat configuration (CCC), and discontinuous cleat configuration (DCC). Even though the mean pressure coefficient values reported in their study were consistent with those of [7]; peak pressure coefficients were significantly higher in magnitude. In this case, peak pressure coefficients of -5.6 and -8.0 were reported on the front and top faces of the coping. In addition to this, the authors also evaluated peak pressure coefficients with a 78% probability of non-exceedance from a Gumbel distribution fitted to the field data. Based on this evaluation, peak pressure values of -3.1 and -4.6 for the front and top faces of the coping, respectively, were suggested to be used in the NBCC. The authors also recommended the usage of roof components and cladding provisions for the conservative design of edge metal systems.

The load demand reported by previous studies is higher than those recommended by current design and testing standards such as ASCE 7–22 [10] and ANSI/SPRI/FM 4435/ES-1 [11], respectively. [8] highlighted the need to evaluate design loads for standards that use the 3-s time averaging scheme for peak loads. A comprehensive wind tunnel study that takes advantage of the current state of the art to investigate wind effects on edge metal systems is also missing in the body of knowledge. Furthermore, as opposed to previously investigated cases, edge metals can experience significant wind-induced vibrations even at relatively low wind speeds which may result in an increased wind loading [12,13]. Resonant vibrations can significantly affect the performance of edge metals and roof membranes under strong winds leading to their damage and possible water intrusion into the building's interior. While previous studies have investigated dynamic effects on rooftop and ground-mounted PV arrays [14–17], and claddings [18,19] using full- and large-scale wind tunnel testing, no research has been conducted so far to examine such dynamic effects on edge metals. In addition, the criterion for dynamically sensitive structures defined by ASCE 7–22 [10] as having a fundamental natural frequency ≤1 Hz, applies to buildings and not to building components. This further highlights the need to account for wind-induced dynamic effects in the design of edge metals.

To overcome these limitations and fill major knowledge gaps in the wind loading of roofing edge metal systems, the objective of this study is to investigate the aerodynamics and wind performance of roof edge metal systems. This paper presents findings from a full-scale experimental campaign using a state-of-the-art wind tunnel. The experimental procedure, which involves aerodynamic, dynamic, and failure assessment tests, is described in the first section. The second section discusses results obtained from pressure and acceleration measurements on the roof system, as well as failure mechanisms obtained from destructive tests. In addition, this section presents a comparison of the measured wind loads from this study with those found in the literature, and current building codes and standards. Finally, the last section summarizes the study's findings and provides recommendations that can help inform the design of more wind-resistant edge metal systems.

2. Experimental methodology

Full-scale experimental tests were conducted at the 12-fan Wall of Wind (WOW) Experimental Facility (EF) at Florida International University (FIU). The WOW EF is a part of the National Science Foundation's (NSF's) Natural Hazards Engineering Research Infrastructure (NHERI). The WOW is a large-scale open-jet experimental facility that can simulate wind speeds and turbulence characteristics like those observed in a Category 5 hurricane on the Saffir-Simpson scale with wind speeds up to 70 m/s (157 mph). The flow field of the WOW is 4.3 m high, 6.1 m wide, and 9.8 m downstream of the contraction zone, and is conditioned with spires and roughness elements that can help generate the desired atmospheric boundary layer profile [20,21]. This section discusses the experimental testing procedure which consists of (1) the building model and instrumentation, (2) the testing protocol, and (3) data analysis.

2.1. Building model and instrumentation

Flat-roofed building models, measuring 3.35 m (W) x 3.35 m (L) and 1.75 m (H), were constructed on-site at the WOW by certified roofing contractors. The constructed roof decks were then sequentially covered with underlayment, Polyisocyanurate (ISO), and

Thermoplastic Polyolefin (TPO) roofing membrane [see Fig. 1]. The membranes were then secured along the roof perimeters using galvanized fasteners and standardized edge metal systems consisting of 24- and 22-gauge stainless steel fascia and cleat, respectively. To consider the current and most common industry practices, four different cleat and nailing configurations were used on their respective flat roof decks. As shown in Fig. 2a and b, the first two configurations consisted of 15 cm (6-in) tall cleats fastened to the substrate at a distance of 4.4 cm (1.75 in) and 11.4 cm (4.5 in) from the lower end, respectively. The second pair of edge metal systems consist of taller cleats that extend up and over the roof surface and help hold the membrane down along with the fascia [see Fig. 2c and d]. For Configurations 3 and 4, the cleats were nailed horizontally and vertically at a distance of 1.9 cm (0.75 in) from the roof edge, respectively. For all four configurations, fasteners were placed along the building's length and width at a 15 cm (6 in) center-to-center spacing.

Pressure taps, connected to a ZOC33/DSM4000 Scanivalve data acquisition system, were used in this study to measure the wind-induced pressures on the roof membrane and the edge metal system. The distortions in amplitude and phase of the measured pressures due to tubing lengths were corrected using appropriate transfer functions [22]. In addition, Dytran accelerometers (full-scale range of $\pm 500 \text{ m/s}^2$) were used to measure the system's response and capture wind-induced dynamic effects. Due to the symmetrical square roof shape, where similar wind effects are expected on all four corners of the building, only one corner of each roof deck was selected for instrumentation. Specifically, the southwestern corner of each deck was instrumented with 58 pressure taps and two accelerometers, as illustrated in Fig. 3. The instrumentation consisted of two groups of pressure taps: the first group was installed on the external surfaces of the TPO membrane and fascia, whereas the second group was installed in the cavities, which are located (1) between the cleat and the substrate, (2) between the fascia and the cleat, and (3) between the TPO and the ISO (Fig. 3a and b). External and internal pressure taps on the edge metal were placed 7.5 cm (5 in) below the roof edge. The corner pressure taps were placed at 15 cm (6 in) from their respective edges and the remaining taps were installed at 30.5 cm (12 in) spacing (i.e., 15 cm offset from fasteners). Furthermore, the two accelerometers were installed at the corner and mid-span of Edge Metal (EM) 1 for all four configurations, as shown in Fig. 3. Each of the two accelerometers was installed at the bottom surface of the fascia's drip edge [see Fig. 3b].

2.2. Testing protocol

Aerodynamic experiments were conducted at mean wind speeds of 11.7, 23.5, 31.3, 35.4, and 39 m/s (26.2, 53, 70, 79.2, and 87 mph) at the mean roof height of 1.75 m (5.7 ft) using simulated open terrain flows for a roughness length of $z_0 = 0.07$ m. The acquisition of acceleration data, within the accelerometers' range, was limited to mean wind speeds of 11.7, 23.5, and 31.3 m/s. Both pressure and acceleration data were sampled for 60 s at a sampling rate of 500 Hz for 24 wind directions, θ (i.e., 0° –345°). Due to the large model scale, the high-frequency component of the full wind spectrum was simulated during the experiments, whereas there was a deficit in the low-frequency turbulence [see Fig. 4]. The effects of the missing low-frequency turbulence on the wind loading were incorporated in the post-test Partial Turbulence Simulation (PTS) analysis [23,24]. The PTS approach is based on the assumptions of the quasi-steady aerodynamic theory and its accuracy has been previously validated by Refs. [23,24] by comparing peak pressure coefficients obtained from the WOW, after PTS correction, with the field measurements on Silsoe cube [25,26] and Texas Tech University's (TTU's) WERFL building [27,28]. In addition to aerodynamic tests, high-speed failure assessment tests were also performed at 3-sec gust speeds which were increased from 43 m/s (96.2 mph) with increments of 3.5 m/s (7.8 mph) until the edge metal failure for the three principal wind directions (0°, 45°, and 90°) and using similar terrain exposures.

2.3. Data analysis

The pressure coefficients (C_p) were computed using Equation (1), where $\Delta P(\theta,t) = P(\theta,t) - P_o(t)$ is the relative differential pressure at the tap location, and \overline{U}_{ref} corresponds to the mean wind speed at the mean roof height. $P(\theta,t)$ is the measured fluctuating pressure time series while $P_o(t)$ is the static reference pressure measured using Scanivalve static bottle that is positioned outside the wind tunnel



Fig. 1. Full-scale building model on WOW EF turntable.

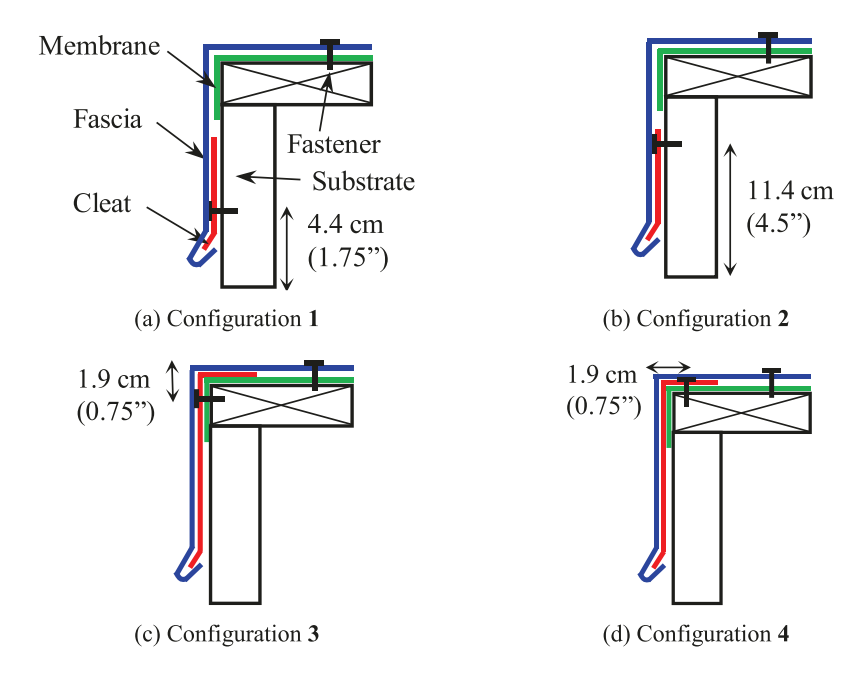


Fig. 2. Edge metal configurations.

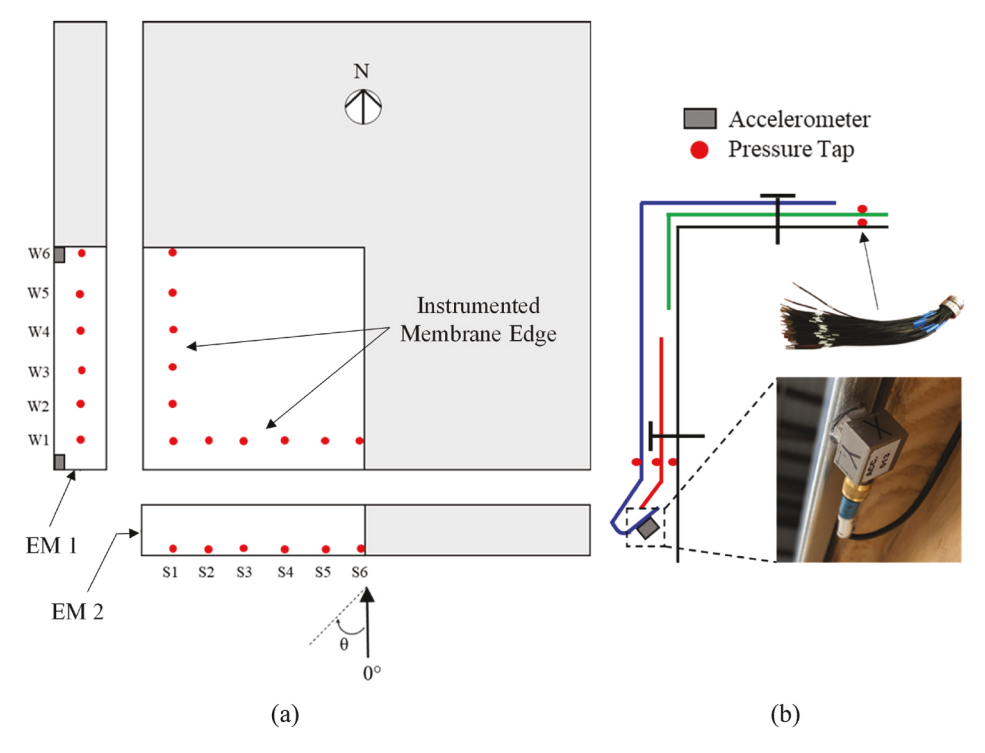


Fig. 3. Instrumentation layout (a) top view; (b) cross-section (Configuration 1).

with controlled temperature and humidity. Consequently, mean and peak pressure coefficients (i.e., \overline{C}_p and \widehat{C}_p) were computed as described by Equations (2) and (3). The PTS method was used to compensate for the missing low-frequency turbulence effects in full-scale testing. Using the PTS approach, the pressure coefficient time series were divided into N = 100 independent subintervals and \widehat{C}_p were estimated based on Extreme Value distribution (i.e., Fisher Tippet Type I fit) for a 1-h full-scale storm duration. The missing low-frequency turbulence intensity was $I_{uL}=23\%$, the target probability of non-exceedance was $P_N=0.78$, and the probability of

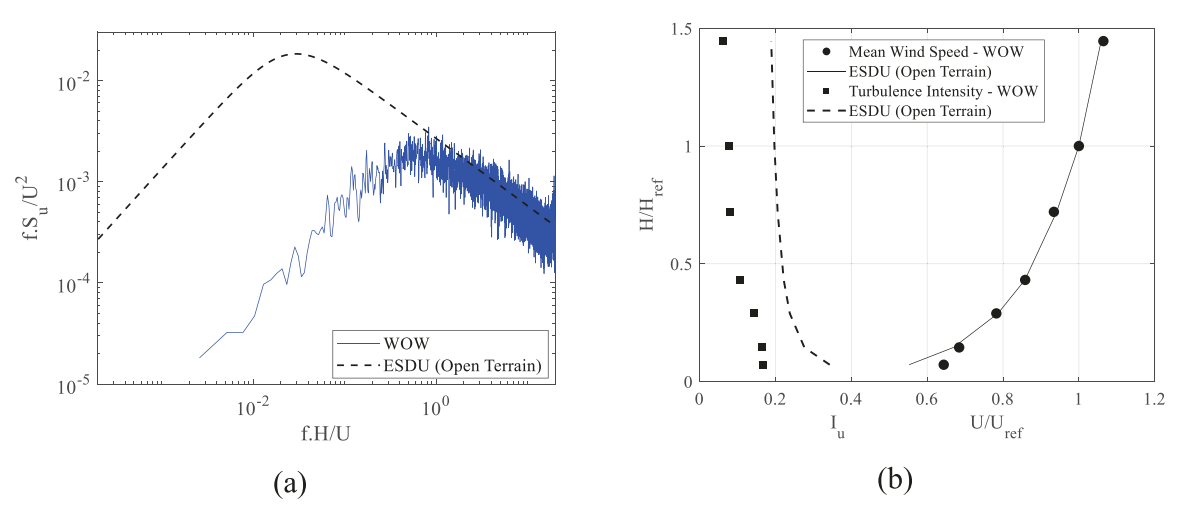


Fig. 4. (a) Von Karman and WOW wind spectra at mean roof height (b) open terrain profile.

exceedance per subinterval was $G = 3.08 \times 10^{-5}$. It should be noted that, for direct comparison with ASCE 7–22, the \widehat{C}_p values were normalized by the 3-sec gust speeds \widehat{U}_{3s} , evaluated using Equation (4) where \overline{U}_{3600s} is the mean hourly wind speed.

$$C_p(\theta, t) = \frac{\Delta P(\theta, t)}{0.5 \, \rho \, \overline{U}_{ref}^2} \tag{1}$$

$$\overline{C}_{p}(\theta) = \frac{\overline{\Delta P}(\theta)}{0.5\rho \,\overline{U}_{ref}^{2}} \tag{2}$$

$$\widehat{C}_{p}(\theta) = \frac{\widehat{\Delta P}(\theta)}{0.5 \rho \widehat{U}_{3_{s}}^{2}}$$
(3)

$$\frac{\widehat{U}_{3s}}{\overline{U}_{3600s}} = 1 + 3.4 \, I_U \tag{4}$$

The measured acceleration data were used to obtain the dynamic properties of the edge metal system. Specifically, the natural frequency n_0 and damping ratio ζ were computed from the acceleration time histories for the various wind speeds using the Random Decrement Technique (RDT) [29–31]. The obtained dynamic properties were then used to analytically incorporate the wind-induced dynamic effects in the measured force coefficient time history $C_F(\theta,t)$ [see Equation (6)] while accounting for the missing low-frequency turbulence, as described in Ref. [15]; and [16]. The Mechanical Admittance Function $|H(n)|^2$, shown in Equation (5), was used to analytically compensate for the resonant component in the wind loading spectrum.

$$|H(n)|^{2} = \frac{1}{\left[1 - \left(\frac{n}{n_{0}}\right)^{2}\right]^{2} + 4\zeta^{2}\left(\frac{n}{n_{0}}\right)^{2}}$$
(5)

Time history of the compensated wind loading $C_{F(B+R)}(t)$, which includes both the background (B) and resonant (R) components, was then obtained from the compensated spectrum using the Inverse Fast Fourier Transform (IFFT) [15,32]. In addition, a Dynamic Amplification Factor (DAF), which relates $\widehat{C}_{F(B+R)}$ to \widehat{C}_F , was calculated for various wind speeds, as described in Equation (7).

$$C_F(\theta, t) = \frac{\sum_i \Delta P_i(\theta, t) \cdot A_i}{0.5 \,\rho \,\overline{U}_{ref}^2 \cdot \sum_i A_i} \tag{6}$$

$$DAF = \frac{\widehat{C}_{F(B+R)}}{\widehat{C}_F} \tag{7}$$

3. Results and discussion

3.1. Aerodynamic loads on the edge metal system and roof membrane

Results of the aerodynamic tests showed that, for all the evaluated configurations, the edge metals experienced the highest suctions when the wind flows were directed near-parallel to their surface. That is, the highest suctions were recorded on the edge metal corners

for wind flows directed close to 0° (360°) for EM 1 and 90° for EM 2. $\widehat{C}_{p}(\theta)$ values for pressure taps located at the midspan of the edge metals exhibit a more symmetrical distribution about the wind direction normal to the edge metal of interest (e.g. 90° for EM 1 and 0° for EM 2), while values for pressure taps placed at the corners are skewed towards their respective corners. Fig. 5 presents the obtained peak suctions by the six pressure taps (i.e., W1 to W6) placed on EM 1.

Previous studies have reported \widehat{C}_p values corresponding to a normal wind flow to the edge metal [6–8,33]. According to this study's findings, a normal wind direction corresponds to a less critical condition as opposed to near-parallel winds. Specifically, wind flows directed 15° from the axis parallel to each edge metal (towards its corner) were found to cause the highest suctions on the corners of all tested configurations (e.g., $\theta = 15^\circ$ for EM 1 and 75° for EM 2). Figs. 6 and 7 present the most critical external \overline{C}_p and \widehat{C}_p distributions for EM 1 using an exploded view of the instrumented roof quarter. For each configuration, the elevation views of the edge metals are placed along their respective roof edges. In addition, the tributary areas of the pressure taps on the edge metals and roof membrane are represented by rectangular areas. Positive \overline{C}_p values were observed on the windward side while those on the across-wind surface were negative. Critical \overline{C}_p values on the edge metals obtained from these tests were 0.92 and -1.1 for the windward and across-wind directions, respectively. In comparison, \overline{C}_p values on the roof were negative for the entire pressure taps placed on the membrane surface with minimum values reaching up to -3.35 for a cornering wind direction. Consistent with the findings of [8]; negative peak pressure coefficients (\widehat{C}_p) on the edge metal systems were observed even for windward directions. As shown in Fig. 7, high suction values on the fascia were recorded at the corner tap locations for all four configurations. The highest suctions were recorded on Configuration 4 (see Fig. 7d), the case with the highest degree of flexibility. Specifically, the highest \widehat{C}_p values in magnitude were -3.2, -3.1, -3.3, and -3.9 for Configurations 1, 2, 3, and 4, respectively.

The dual aerodynamic nature of edge metal systems (i.e., roof- and wall-like characteristics) can be observed from these results. For all four configurations, mean positive pressures were acting on the windward sides of the roof and suctions on the across-wind sides, as expected on the wall surfaces of buildings. Besides peak suctions being evident on the windward sides, different interactions with roof

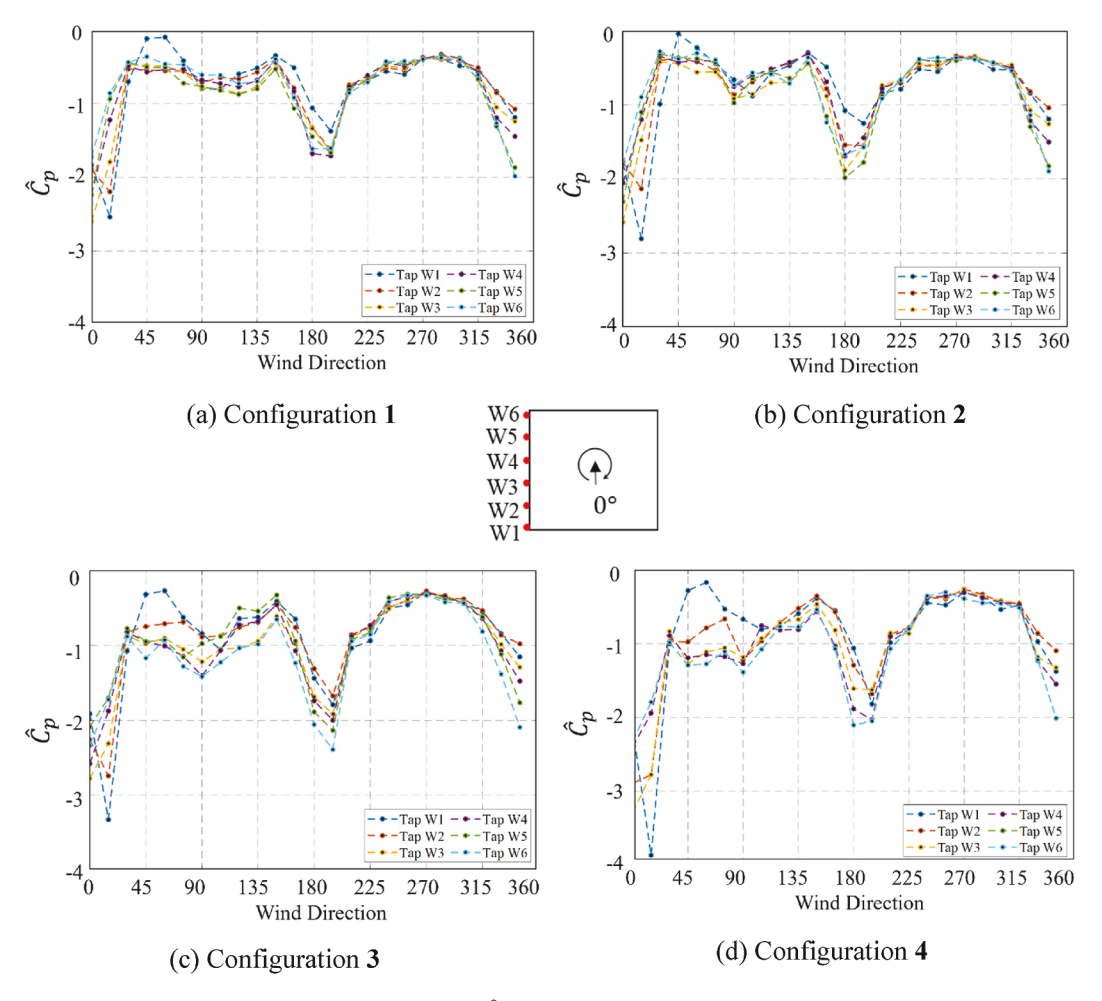


Fig. 5. Directional \widehat{C}_p for pressure taps placed on EM 1.

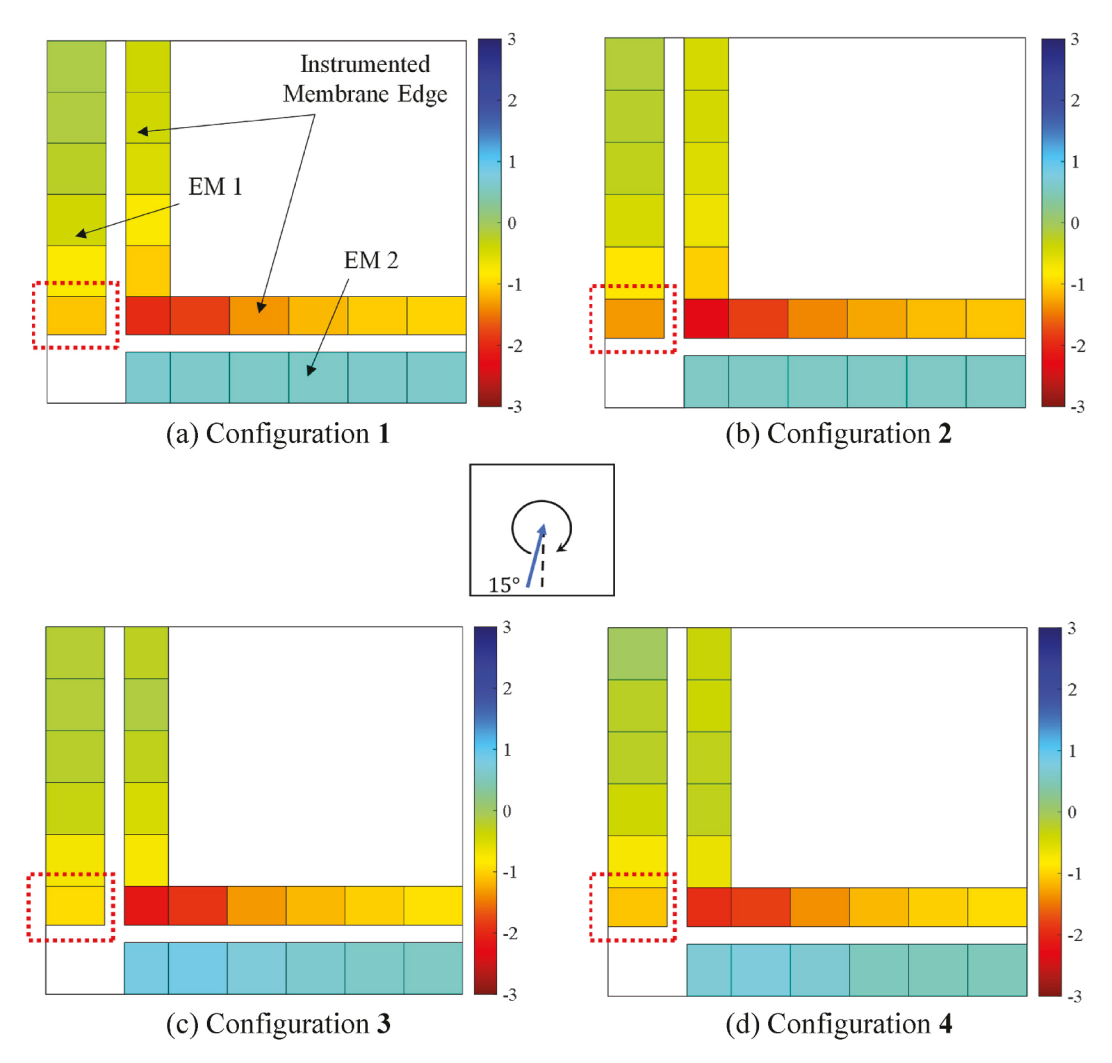


Fig. 6. \overline{C}_p distribution on the roof edge and fascia.

loading can be observed. That is, for Configurations 1 and 2, where the cleats are fastened to the substrate at their lower ends, peak pressures observed on the fascia for the critical wind direction were significantly lower than the roof suctions [see $\widehat{C}_p(15^\circ)$ in Fig. 8 (a, b)]. On the contrary, for Configurations 3 and 4 where the cleat fasteners at the top facilitate a greater degree of vibration, peak pressures on the fascia are found to be similar to those observed on the roof [Fig. 8 (c, d)]. This implies that the more these edge metal systems are lifted by the wind (i.e., Configurations 3 and 4), the more exposed they are to roof-like pressures. Conversely, when these systems are restricted from vibrating (i.e., Configurations 1 and 2), wall-like loading conditions factor in.

In addition to external surface pressures discussed thus far, cavity pressures were also investigated at three locations: (1) between the fascia and cleat, (2) between the cleat and substrate, and (3) between the TPO and polyisocyanurate. Considering these cavity flows, two net pressures on the edge metal system and one on the membrane were computed. The first net pressure coefficient, $C_{p_{net_1}}$, corresponds to the pressure on the fascia that acts to disengage it from the cleat and is therefore computed as the algebraic difference between pressure coefficients recorded on the front and back sides of the fascia, as shown in Equation (8). When the edge metal system is acting as a unit (i.e., fascia and cleat are engaged), the net pressure that acts to lift the system, $C_{p_{net_2}}$, is the algebraic difference between pressure coefficients recorded on the front of the facia and the back of the cleat [see Equation (9)]. The net pressure on the membrane $C_{p_{net_2}}$ is similarly computed using C_p values recorded on the top and bottom sides of the TPO, as shown in Equation (10).

$$C_{p_{net_1}}(\theta, t) = C_{p_{fascia}}(\theta, t) - C_{p_{clear}}(\theta, t)$$
 (8)

$$C_{p_{net}}(\theta, t) = C_{p_{fincts}}(\theta, t) - C_{p_{substrate}}(\theta, t)$$
 (9)

$$C_{P_{REI}}(\theta, t) = C_{PTPO}(\theta, t) - C_{PISO}(\theta, t)$$
(10)

Cavity pressures were observed to cause net wind load escalation and reduction depending on the wind direction and pressure tap

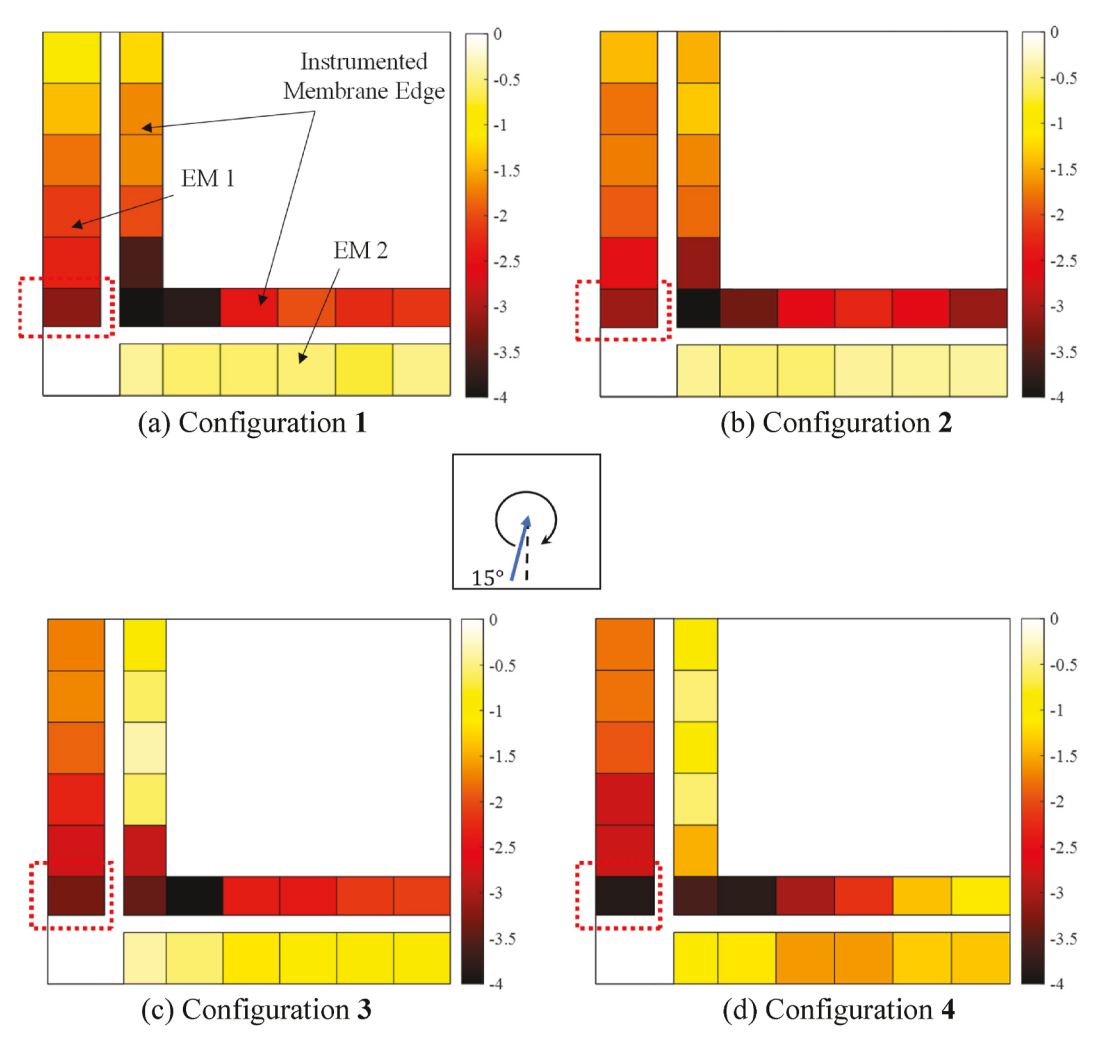


Fig. 7. \widehat{C}_p distribution on the roof edge and fascia.

location. For wind directions that are predominantly normal to the fascia surface, cavity pressures between the facia and the cleat, and those between the cleat and substrate were mostly positive, adding to the suction on the fascia's external surface. That is, the ratio of net to peak external C_p values is greater than unity. Note that these ratios may get significantly high for areas subjected to low external suction (close to 0). On the other hand, these ratios tend to be lower for near-parallel wind directions, where cavity flows were observed to increase or reduce the net pressure depending on the measurement location. The reduction in net pressure, in this case, was observed to be as much as 50% in some cases. Moreover, net-to-peak external C_p ratios were found to vary with edge metal configurations used. While an increase in the critical peak net pressure coefficients was recorded for Configurations 2 and 3, a significant reduction was observed for Configuration 1. Critical $\widehat{C}_{p_{net_1}}$ and $\widehat{C}_{p_{net_2}}$ values for Configuration 3 were 19% and 4% higher in magnitude, respectively, compared to the \widehat{C}_p on the same fascia. The increase in the critical $\widehat{C}_{p_{net}}$ values were within 5% for Configuration 2. In contrast, critical $\widehat{C}_{p_{net_1}}$ and $\widehat{C}_{p_{net_2}}$ values for Configuration 1 were lower in magnitude by 10% and 20% compared to \widehat{C}_p on the same system. For Configuration 4, however, critical $\widehat{C}_{p_{net_1}}$ increased in magnitude by 2% while critical $\widehat{C}_{p_{net_2}}$ reduced by 12%. Furthermore, net suctions that are responsible for the disengagement of the fascia from the cleat $(\widehat{C}_{p_{net_1}})$ were generally found to be higher than those that act to lift the fascia and the cleat together $(\widehat{C}_{p_{net_2}})$. $\widehat{C}_{p_{net_1}}$ values for pressure taps placed on EM 1 are shown in Fig. 9 while their $\widehat{C}_{p_{net_2}}$ counterparts are shown in Fig. 10.

Comparing the experimental results from this study with field investigations conducted by Ref. [8] showed a reasonable agreement for similar configurations and wind directions. The edge metal configurations considered in Ref. [8] resemble Configurations 1 and 2 from the current study for normal and oblique wind flows. As discussed earlier, the study reported hourly critical peak net C_p values of -5.6 on the front faces of an edge metal system. In the current study, the critical 3-s peak net C_p value for wind directions ranging from normal to oblique is -1.7, converted to an hourly peak using Equation (4) is a value of -5.7. When considering Configuration 3 and 4,

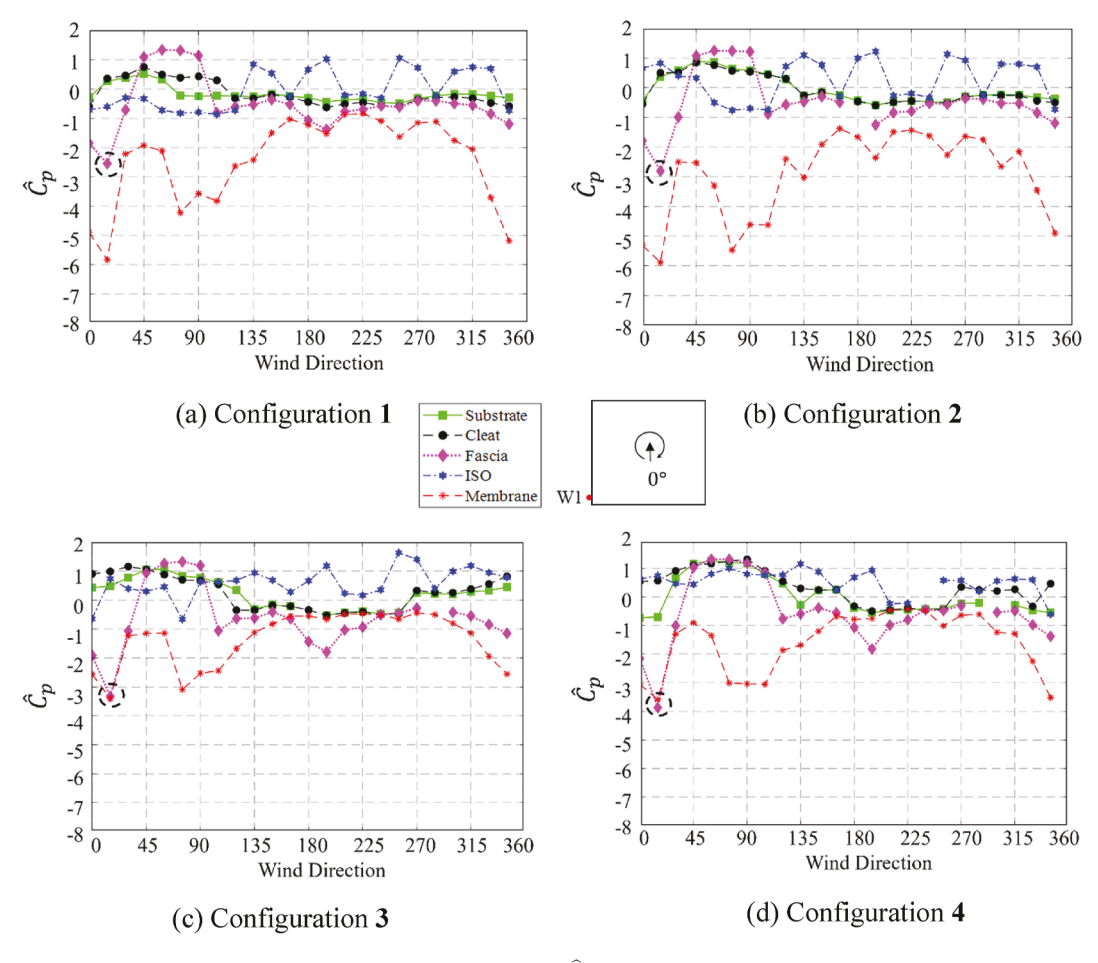


Fig. 8. Directional \widehat{C}_p for tap W1.

critical peak values obtained in this study are higher in magnitude even for similar wind directions. The critical 3-s peak net C_p obtained for a normal wind direction on Configuration 3 was -2.0, equivalent to an hourly peak net C_p of -6.7, which is 16% higher than that reported by Ref. [8]. In addition, for near-parallel wind directions not considered by Ref. [8]; these values reach up to a 3-s peak net C_p of -3.98 (hourly peak of -13.35).

Area-averaged pressures on the edge metal systems were evaluated in the current study to compare with the current ES-1 design requirements [11]. ES-1 calculates design loads by using External Pressure Coefficients (GC_p) values of -0.97 and -1.21 for fascia perimeters and corners, respectively, for building heights less than 60 feet (18.2 m). For heights higher than 60 feet (18.2 m), ES-1 uses perimeter and corner GCp values of -0.68 and -1.25, respectively. These values are obtained from ASCE 7–10 component and cladding GCp provisions (Figs. 30.3–1) with the recommended 10% reduction for roof slopes less than 10° [see Fig. 11] [34]. Note that the GC_p values shown for this case were unchanged in subsequent editions, i.e., ASCE 7–16 and ASCE 7–22 [10,35].

The peak area-averaged net pressure coefficients $\widehat{C}_{p_{met}av}$ were computed from their corresponding time histories $C_{p_{net}av}(\theta,t)$ using Equation (11), where A_i represents the tributary area for the i^{th} tap. Following the area zonings provided in ASCE 7–22 [10], area-averaging was conducted for the corner (C) and mid-span (M) areas for combinations of 2 and 3 taps for each case [see Figs. 12 and 13]. Selecting a maximum of three taps for area-averaging is consistent with the ASCE 7 zonal classification shown in Fig. 11, where the width a for zone 5 is 3 feet (0.9 m). The results from this study showed that critical corner area-averaged values can reach up to -2.0 and -1.5 for corner and mid-span regions of the roof, respectively, for parallel and near-parallel wind flows. Area-averaged values for these critical loading cases on EM 1 installed using Configuration 3 are shown in Figs. 12 and 13. Similarly, minimum peak area-averaged values for Configurations 1, 2, and 4 for corner regions were -1.4, -1.7, and -1.6, respectively, while their mid-span counterparts were -1.3, -1.2, and -1.1, respectively. These values are higher in magnitude than those currently used for conducting ES-1 tests and those provided in ASCE 7–22. Moreover, using area-averaged loads provided in ASCE 7–22 may not be accurate for edge metal systems as they are located in the uppermost part of the wall and have relatively narrower widths, resulting in a more concentrated wind load around the corners.

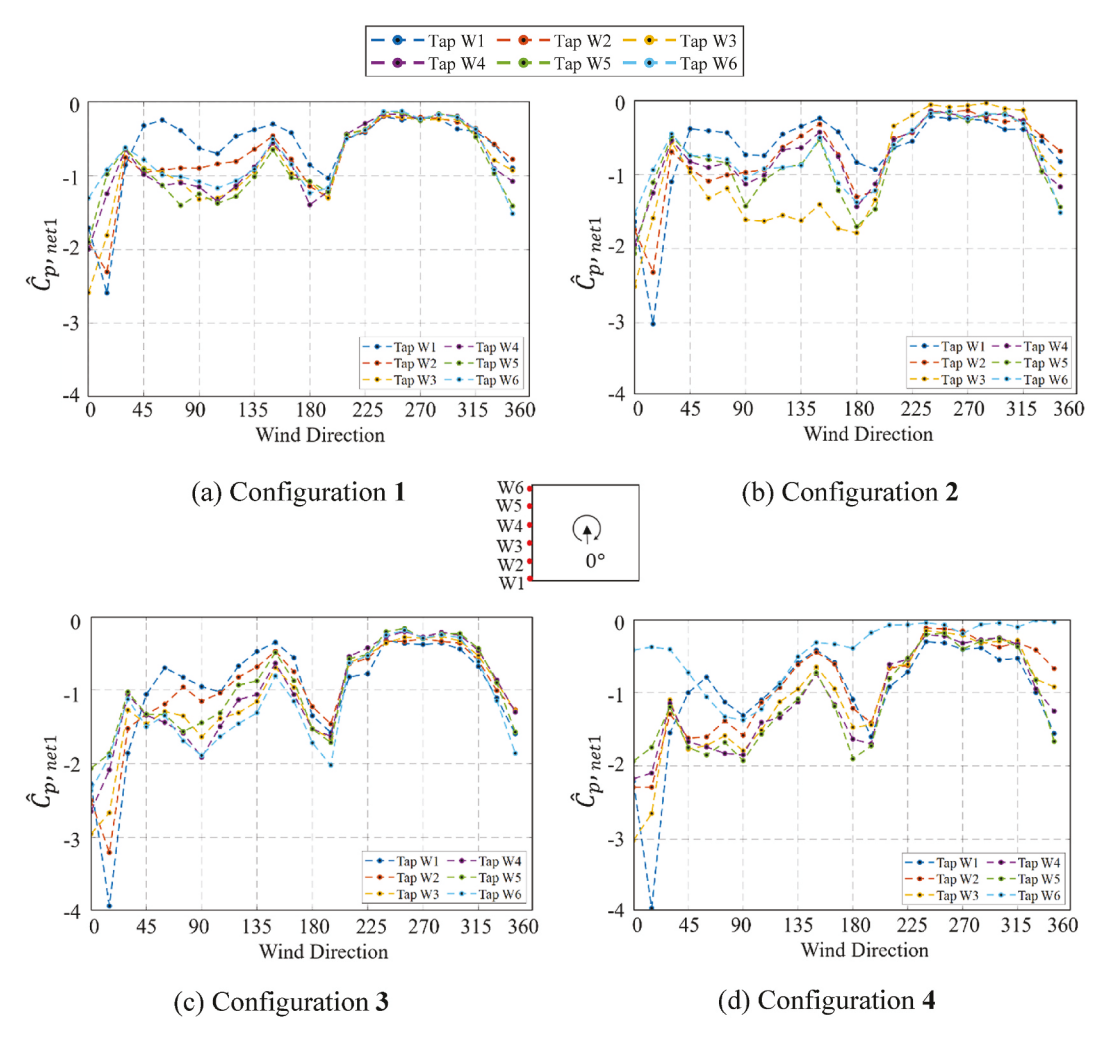


Fig. 9. Directional $\widehat{C}_{p_{net_1}}$ for pressure taps placed on EM 1.

$$C_{p_{av}}(\theta, t) = \frac{\sum_{i} C_{p_i}(\theta, t) A_i}{\sum_{i} A_i}$$
(11)

This study also showed that the edge metal configurations used on the roof edges have a direct influence on roof pressures. Besides the similarity between the suctions observed on the fascia and the roof edge as discussed earlier for Configurations 3 and 4, suctions on the roof decks installed using these two methods were also observed to be significantly lower than those on Configurations 1 and 2. Fig. 14 presents directional $\hat{C}_{p_{net3}}$ plots for the six pressure taps located on the western edge of the roof.

The results presented therein show that the relative flexibility of the edge metal system has changed both the magnitude and the distribution of peak loads over the roof surface. While critical values for Configurations 1 and 2 can be seen to be close to -6.0, those on Configurations 3 and 4 were generally higher than -4.0, about a 25% reduction in peak Cp. This is likely due to two possible reasons: (1) wind flows separating from the lower ends of the fascia than the roof edges as the edge metal system acts as an extension of the roof and thus shortening the length of the separation bubble; (2) fascia vibrations altering the rooftop separation bubble. Similar to roof edge and parapet aerodynamic modifications used to reduce rooftop suctions, allowing a higher degree of flexibility for edge metal systems may also be used to achieve the same goal [36–38].

3.2. Wind-induced dynamic effects

The collected acceleration data were used in conjunction with the force coefficient data to identify the dynamic properties of edge metal systems and analytically incorporate the wind-induced resonant component in the wind loads [15,16]. Fig. 15 shows the acceleration spectra on the midspan of the edge metal system for the four configurations at 23.5 m/s (53 mph). It was observed that the natural frequency of the system was the highest for Configuration 1 and the lowest for Configuration 4. More specifically, the natural frequencies of the first mode of vibration were found to be 43, 33, 19, and 10 Hz for Configurations 1, 2, 3, and 4, respectively. This is mainly due to the dependence of the system's flexibility for each configuration on the cleat anchorage location. For instance, a cleat

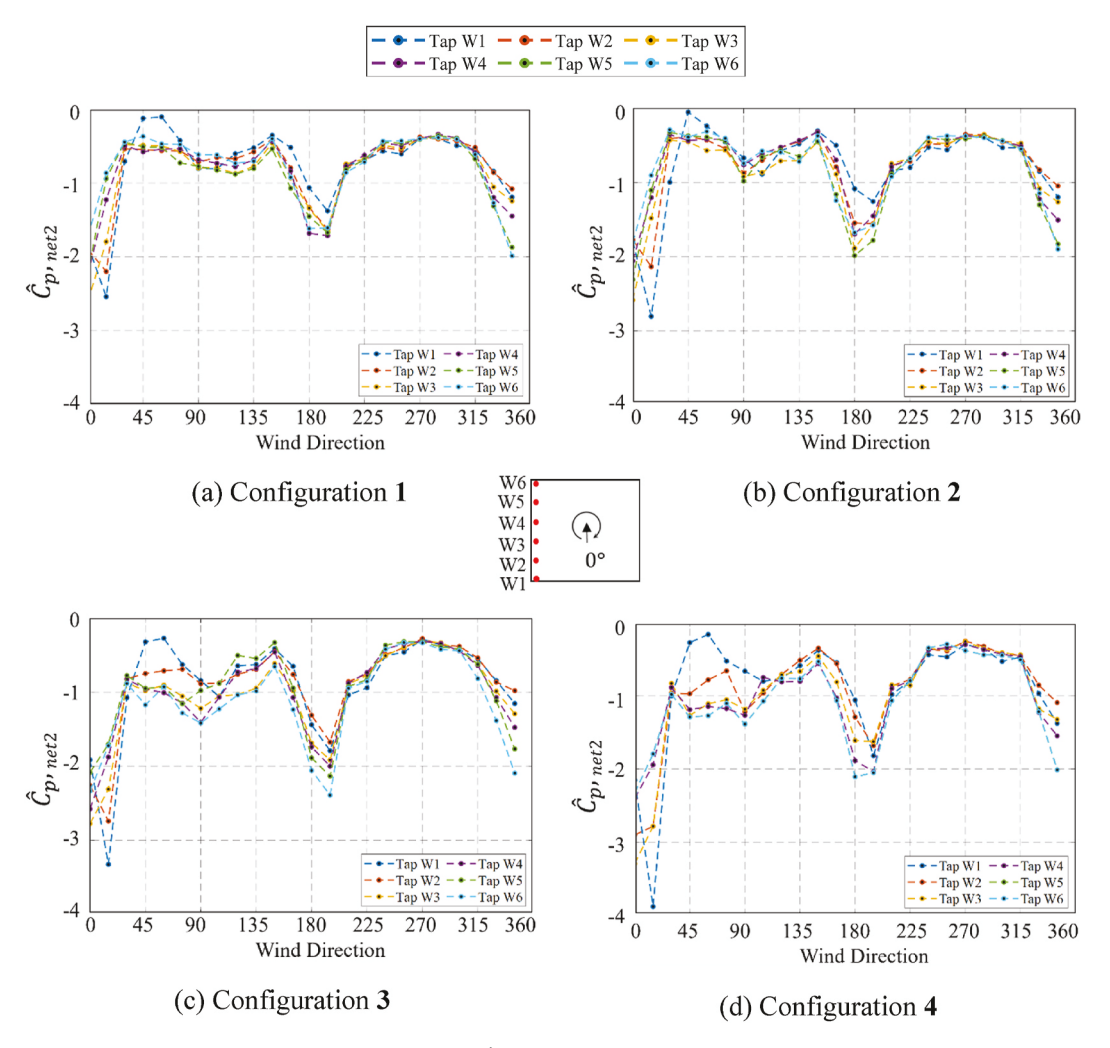


Fig. 10. Directional $\widehat{C}_{p_{\mathrm{net}_2}}$ for pressure taps placed on EM 1.

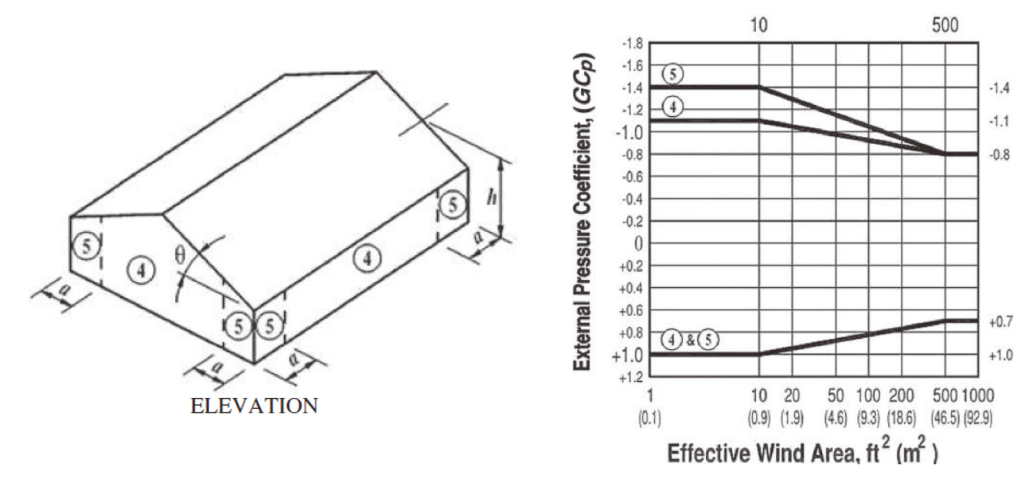


Fig. 11. ASCE 7–22 area-averaged GC_p provisions for walls [10].

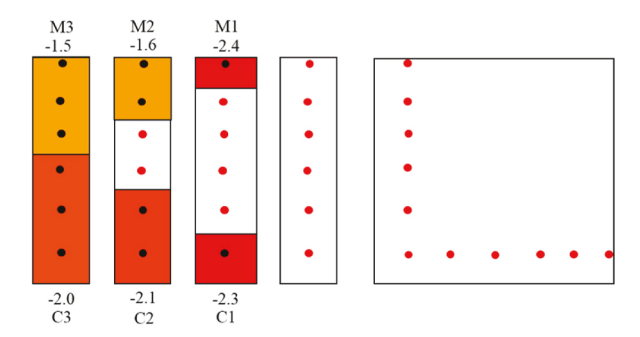


Fig. 12. Area-averaged $\widehat{C}_{p_{net}}(\theta=0^{\circ})$ on EM 1 installed using Configuration 3.

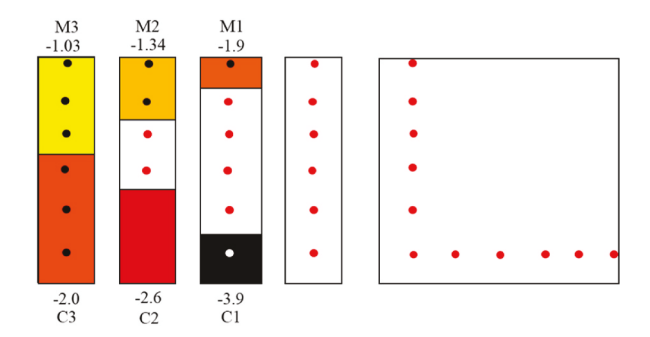


Fig. 13. Area-averaged $\widehat{C}_{p_{nr}}(\theta=15^{\circ})$ on EM 1 installed using Configuration 3.

fastener close to the lower end (Configuration 1) will exhibit a shorter moment arm than the rest of the configurations, which leads to an increase in the stiffness and, consequently, the natural frequency. In contrast, Configuration 4 was subjected to a higher degree of flexibility due to the longer moment arm, which justifies its low natural frequency compared to the other configurations. Besides the natural frequency, the computed damping ratio using RDT was found to be 6%.

The peak accelerations a_{max} for the corner and midspan zones of the four configurations are displayed in Fig. 16 as a function of wind speed and direction. The comparison reveals that the system's flexibility is dependent on edge metal configuration. For example, the highest a_{max} of 130 m/s² was observed at 31.3 m/s for Configuration 3 followed by Configurations 4 and 1 ($a_{max} = 80 \text{ m/s}^2$), then Configuration 2 ($a_{max} = 50 \text{ m/s}^2$). In addition, the highest peak accelerations for Configurations 1 and 3, which were detected at critical near-normal and near-parallel wind directions, are higher at the corner than at midspan. This indicates that Configurations 1 and 3 become more flexible as the wind speed increases due to possible edge metal deformation and failure initiation near the corner, which makes the system susceptible to significant wind-induced vibrations.

The acceleration spectra for the critical wind directions and locations on the four edge metal configurations are presented in Fig. 17 for 31.3 m/s. It was observed that the natural frequency of the edge metal system can be affected by the tested wind speed. Specifically, while no differences were observed in the natural frequencies of Configurations 2 and 4 between 23.5 m/s and 31.3 m/s, those of Configurations 1 and 3 at 31.3 m/s were found to be 15 Hz and 6 Hz, respectively, as opposed to 43 Hz and 19 Hz at 23.5 m/s. It should be noted that the acceleration data could not be captured at wind speeds higher than 31.3 m/s due to limitations related to the accelerometers' measurement range.

The obtained dynamic properties of the four edge metal configurations were used to analytically compensate the force coefficient spectrum for dynamic effects, as shown in Fig. 18 for Configuration 3. The DAF was evaluated for two scenarios: (1) using the initial natural frequencies obtained at lower wind speeds (DAF $_1$ in Fig. 19a); (2) by considering the change in the natural frequency at higher wind speeds due to failure initiation (DAF $_2$ in Fig. 19b). In the second scenario, the initial natural frequencies were used up to a wind speed of 31.3 m/s, where a change in the dynamic properties was observed for Configurations 1 and 3. Even though the system's flexibility is expected to increase with increasing wind speed, the dynamic properties captured at 31.3 m/s were used to characterize the system's behavior during failure initiation.

An increasing relationship between the DAF and wind speed was identified for all configurations, where DAF₁ increased from 1.05 to 1.25 and DAF₂ from 1.05 to 1.4 when the wind speeds were increased from 12 (26.8) to 60 m/s (134 mph). It was observed that upon failure initiation and possible deformation, Configuration 3 became the most flexible system with a DAF of up to 1.4. Dynamic effects were observed to significantly increase the wind loading on edge metal systems, which indicates that not accounting for such effects in the design of these systems may lead to nonconservative results. This implies that edge metal systems may be exposed to significant vibrations at higher wind speeds resulting in much higher wind loads than those obtained at lower wind speeds. In particular, the peak force coefficients $\widehat{G}_{F(R+R)}$ accounting for dynamic effects were found to be as high as -2.50 and -1.90 for the corner and perimeter

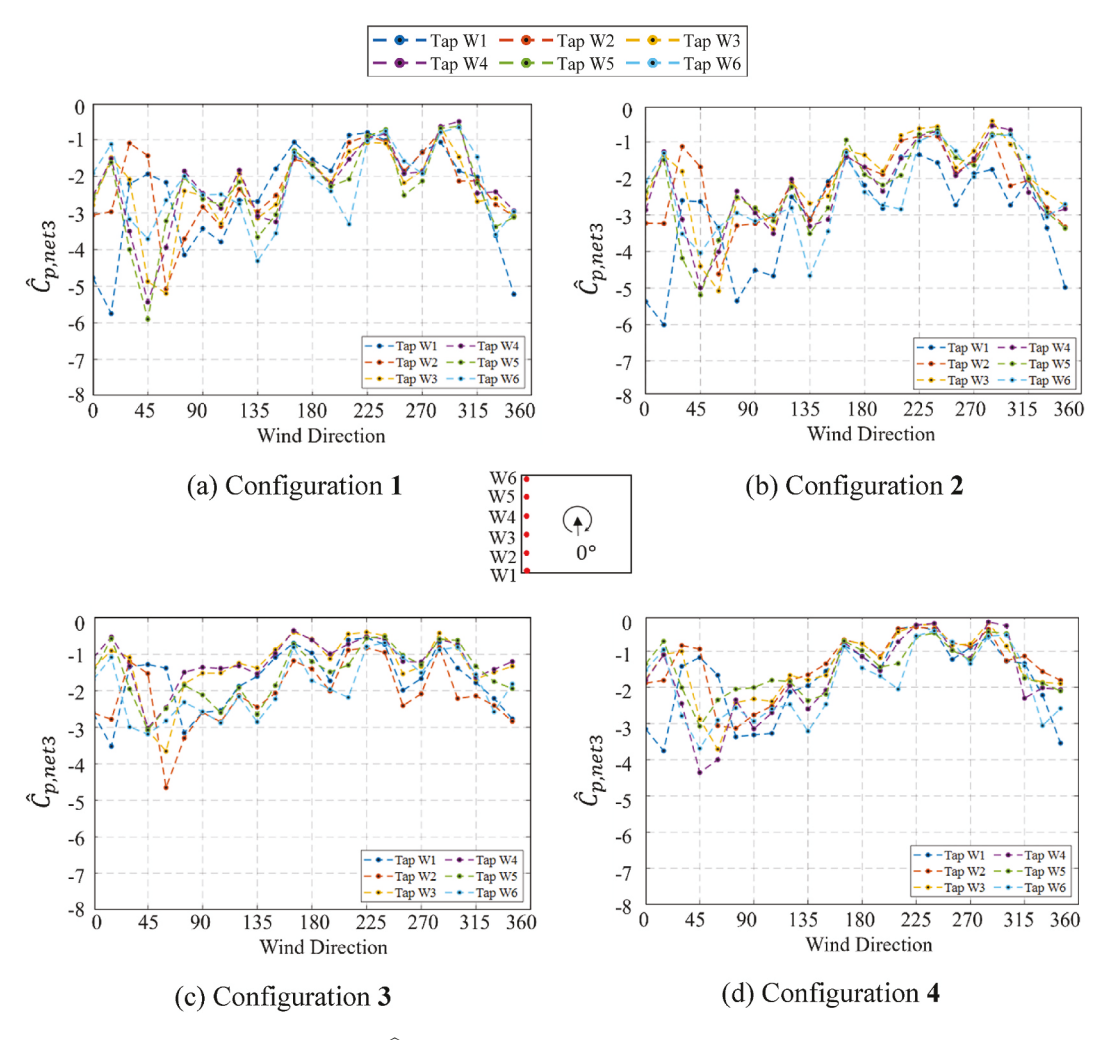


Fig. 14. Directional $\widehat{C}_{p_{net3}}$ for membrane taps placed on the western edge of the roof.

zones, respectively. These values are higher in magnitude that GC_p of -1.1 and -1.4 provided in ASCE 7–22, or -0.97 and -1.21 as used in ES-1 after a 10% reduction [see Table 1].

3.3. Failure assessment results

The failure assessment test results showed an important performance comparison between the four configurations. As expected, the relatively flexible cases (i.e., Configurations 3 and 4), demonstrated wind-compliant oscillation at lower wind speeds compared to Configurations 1 and 2. Interestingly, however, the failure wind speeds were contrary to the current industry knowledge. Configuration 1 was believed to be the most robust among all the four configurations being considered, with the rest following their numberings given in this study. That is, lower fastening of cleats is believed to reduce the exerted lifting moment by reducing the moment arm. Based on this notion, Configurations 3 and 4 were considered susceptible to high lifting moments as the entire thickness (face) of the edge metal system hangs below the fasteners applied. The interesting finding in this study, however, was that the lift-off (i.e., failure) wind speed for all four configurations was similar. It should be noted that, throughout this section, the failure wind speeds correspond to 3-s peaks measured at the roof height. All four edge metal systems were lifted at a wind speed of 60 m/s (134 mph). Fig. 20 shows the edge metal lifting observed for Configurations 2 and 3 at this failure wind speed. In all configurations, lift-offs were initiated at the corners due to near-parallel wind flows, which were consistent with the observations from the aerodynamic study.

Another finding from the destructive test was the susceptibility of Configurations 1 and 2 to installation errors. Premature disengagement of the cleat and fascia was observed for Configuration 1 at a testing wind speed of 31.3 m/s (70 mph) as shown in Fig. 21a. This edge metal system failed (i.e., lifted-off) at a wind speed of 39 m/s (87 mph). This is 35% lower than the wind speed at which the other three configurations lifted off. Examining the reasons for the early disengagement and failure showed that it occurred due to an installation error that placed the cleat slightly higher [about 1 cm (0.4 in)] than its intended location. Such a slight change in the cleat placement resulted in a lack of sufficient engagement between the cleat and fascia drip edge and, consequently, a premature failure. Repeating the test with the correct installation resulted in a similar failure wind speed discussed earlier [i.e., 60 m/s (134)]

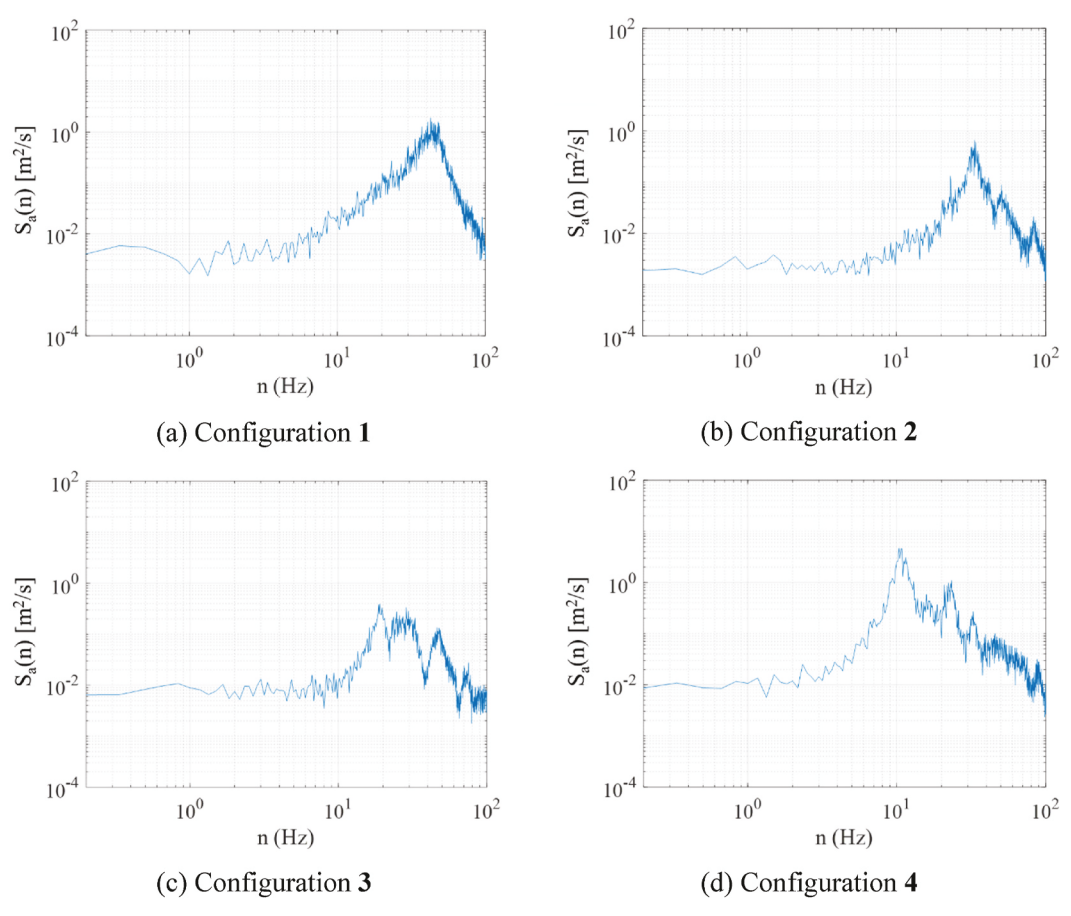


Fig. 15. Acceleration spectra for 23.5 m/s.

mph)]. Based on these findings, achieving the exact engagement length may be improbable given the short length of the drip edge. Since the cleat types, installation procedures, and load-resisting mechanisms are similar for Configurations 1 and 2, similar susceptibility to installation errors can be expected for Configuration 2.

In general, the disengagement of the fascia from the cleat occurs at lower wind speeds for Configurations 1 and 2 than it does for Configurations 3 and 4. For example, even though the lifting (failure) wind speed was 60 m/s (134 mph), the corner areas for Configuration 2 disengaged at a wind speed of 51 m/s (114 mph). In contrast, the edge metals installed using Configurations 3 and 4 did not disengage until the lifting wind speed is reached. Besides the shape of their cleat allowing for a more precise installation, its relative flexibility to vibrate along with the fascia was observed to preserve the fascia-cleat engagement. Fig. 21b shows the cleat engaged and oscillating with the fascia for Configuration 4. The failure assessment results further indicated that low-fastened cleats tend to act more like the substrate, while relatively flexible cleats tend to function as the fascia, providing better dynamic load sharing.

Even though Configurations 3 and 4 are subjected to higher dynamic loads than Configurations 1 and 2 at similar wind speeds, the failure assessment study showed that they have overall better wind resistance. They are less likely to be susceptible to installation errors and showed a better cleat and fascia (e.g., drip edge) engagement that lasted until the edge metal system was lifted. Comparing the edge metal lift-off in Fig. 20b with that shown in Fig. 22, the cleats in Configuration 3 are observed to have not lifted while those of Configuration 4 were completely lifted, exposing the membrane. In this regard, Configuration 3 may be preferable as the cleat will continue to hold the roofing membrane in place and would provide a better shield against water intrusion due to wind-driven rain.

4. Conclusions

This study presents an effort to evaluate wind loads on and responses of edge metal roof elements by considering four configurations commonly used by the roofing industry. This entailed conducting full-scale aerodynamic and failure assessment experiments at the NSF NHERI Wall of Wind (WOW) Experimental Facility (EF) at FIU. The experimental campaign also consisted of investigating the effect of wind-induced vibrations on these systems.

The results showed that fascia elements experience high suctions (negative pressures) due to near-parallel wind flows for all configurations tested, while suctions were found to be higher for relatively flexible configurations by up to 25%. In these cases, the highest suctions experienced by the fascia elements for the critical wind directions were comparable to roof surface peak wind loads.

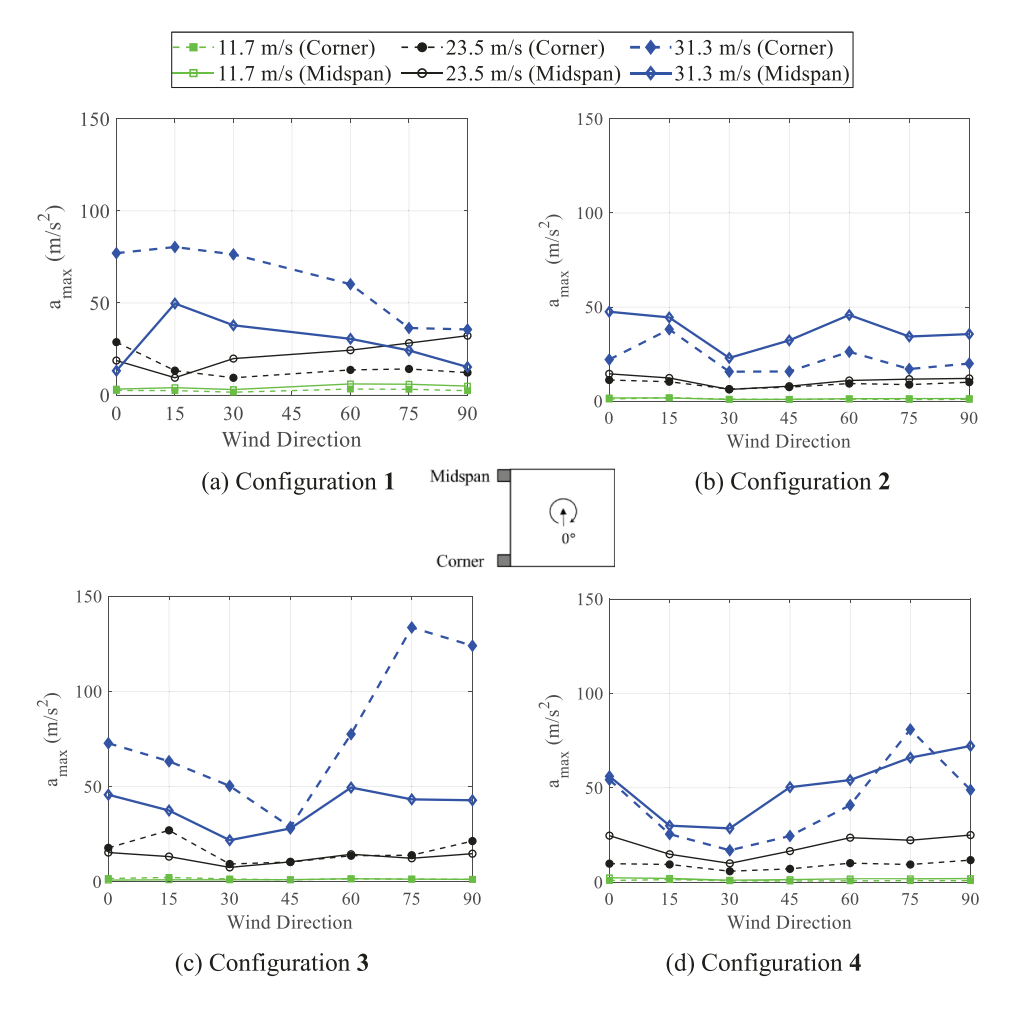


Fig. 16. Peak accelerations on the corner and midspan as a function of wind speed and direction.

Wind flows between the fascia and the cleat, and those between the cleat and the substrate were surmised to cause both an increase and decrease in suction depending on the location of the measurement and wind direction. Generally, an increase in suction was observed for windward directions while the decrease in suction pertained to cases where the wind flows were directed orthogonal to the edge metals. Moreover, peak pressure coefficients were also observed to increase by up to 25% and 40% before and at the onset of failure initiation, respectively, with wind speeds due to increased dynamic contributions. Based on the findings from this study, peak pressure coefficients of -1.9 and -2.5 at the perimeter and corner, respectively, can be used to enhance the design and testing (e.g., ES-1) of edge metal systems.

The study also identified the roof- and wall-like characteristics of the edge metal systems and their relationship to the configuration method employed. Lower nailed cleats were found to act more like the substrate as they did not vibrate along with the fascia. In these cases, the integrity of the fascia was found to be dependent on its engagement with the cleat. The study also showed that configurations with cleats without a horizontal flange are highly susceptible to installation errors that could result in a lack of sufficient engagement length. In contrast, higher nailed configurations with an L-shaped cleat were observed to vibrate with the fascia. Further research is needed to investigate the effect of other geometric parameters of edge metals, such as the drip edge's angle and length, on the wind performance of these systems. In addition, future studies are encouraged to investigate the relationship between edge metal flexibility and aerodynamic pressure on the system as well as fatigue-related effects.

CRediT authorship contribution statement

Ameyu B Tolera: Conceptualization, Formal analysis, Methodology, Writing – original draft, Writing – review & editing. Johnny Estephan: Conceptualization, Formal analysis, Methodology, Writing – original draft, Writing – review & editing. Arindam Gan Chowdhury: Conceptualization, Supervision, Resources, Funding acquisition, Writing – Review & Editing. Ioannis Zisis: Conceptualization, Supervision, Resources, Funding acquisition, Writing – Review & Editing. Erica Sherman: Methodology, Writing – Review & Editing. James Kirby: Methodology, Writing – Review & Editing.

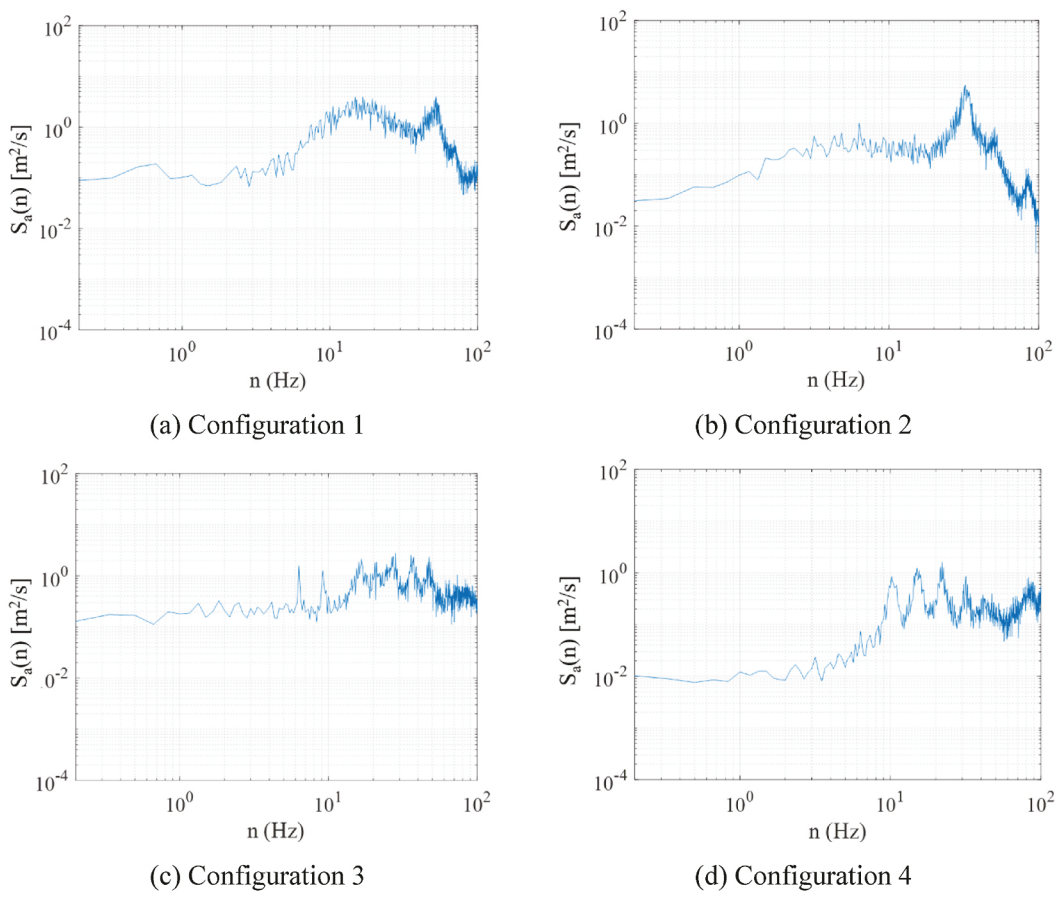
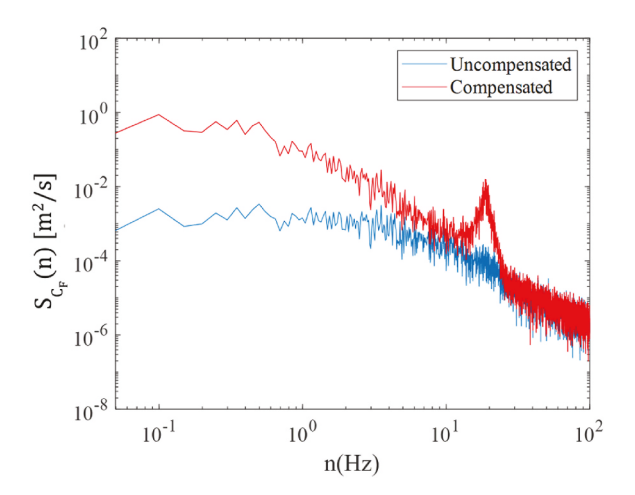


Fig. 17. Acceleration spectra for 31.3 m/s.



 $\textbf{Fig. 18.} \ \ \textbf{Force coefficient spectrum including dynamic effects for Configuration 3.}$

Declaration of competing interest

The authors declare the following financial interests/personal relationships which may be considered as potential competing interests: Arindam Gan Chowdhury and Ioannis Zisis report financial support was provided by National Science Foundation Industry-University Cooperative Research Centers Program. Arindam Gan Chowdhury and Ioannis Zisis report supplies was provided by GAF Materials Corp. Erica Sherman and James Kirby report a relationship with GAF Materials Corp that includes: employment.

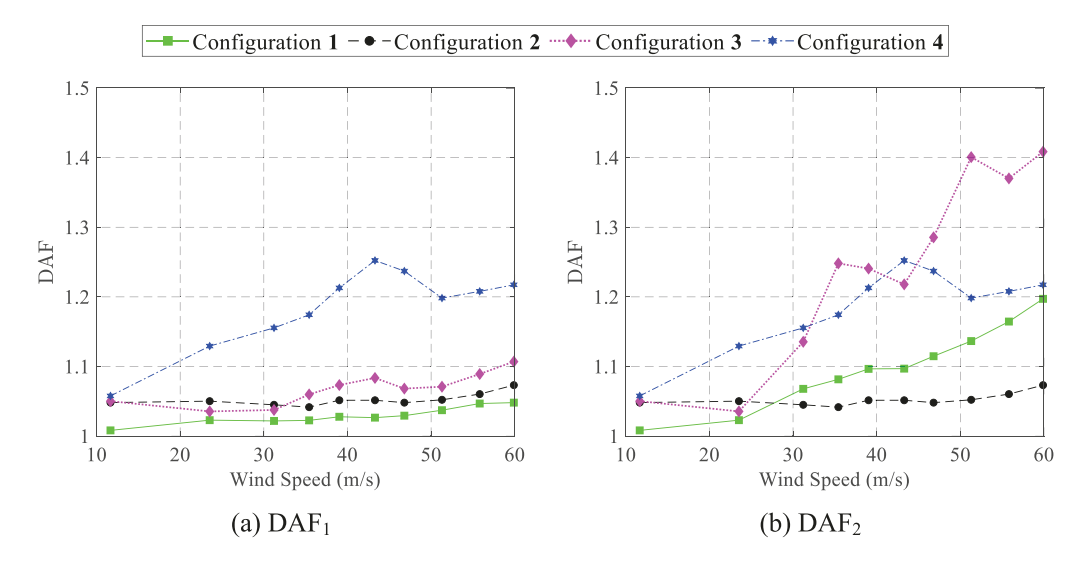


Fig. 19. DAF as a function of wind speed.

Table 1 Comparison of area-averaged peak pressure coefficients with ES-1 test.

	ES-1 Test	Current Test (Aerodynamic)	Current Test (Dynamic)
Perimeter	0.97	1.50	1.90
Corner	1.21	2.00	2.50



Fig. 20. Fascia lifting at a wind speed of 60~m/s (a) Configuration 2, and (b) Configuration 3.



Fig. 21. (a) Configuration 1: premature fascia and cleat disengagement, and (b) Configuration 4: cleat and fascia oscillating together.

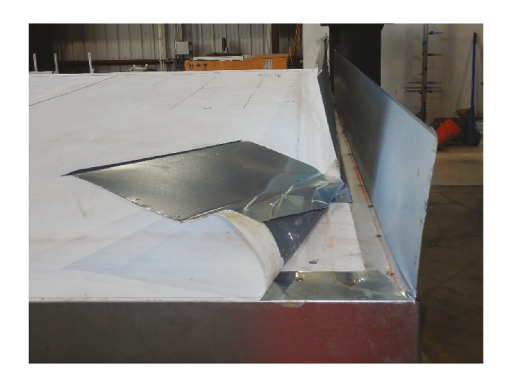




Fig. 22. Fascia and cleat lifting together at 3-sec peak wind speed of 60 m/s - configuration 4.

Data availability

Data will be made available on request.

Acknowledgment

The study was funded by the National Science Foundation (NSF) through the Industry/University Cooperative Research Center (IUCRC) to the Wind Hazard Infrastructure Performance (WHIP) Center at Florida International University (FIU) (award numbers 1520853, 1841503, and 2037899). The authors would also like to thank GAF for providing additional support to cover the expenses of purchasing and installing all the materials needed for the experiment. Ameyu Tolera and Johnny Estephan gratefully acknowledge funding from the Florida International University Graduate School (FIU UGS) Dissertation Year Fellowship (DYF). The experiments were greatly facilitated by the fine work of WOW staff members Dr. Steven Diaz, Walter Conklin, Dr. Dejiang Chen, Roy Liu-Marques, and James Erwin. The opinions, findings, conclusions, or recommendations expressed in this article are solely those of the authors and do not represent the opinions of the funding agencies.

References

- [1] RICOWI, RICOWI Wind Investigation Hurricane Michael, 2018 (Florida).
- [2] RICOWI, Hurricanes Charley and Ivan Wind Investigation Report, 2006.
- [3] RICOWI, Hurricanes Ike Wind Investigation Report, 2009.
- [4] A. Baskaran, S. Molleti, D. Roodvoets, Understanding low-sloped roofs under hurricane charley from field to practice, J. ASTM Int. (JAI) 4 (10) (2007) 3–15, https://doi.org/10.1520/JAI101055.
- [5] T. Smith, Hurricane hugo's effect on metal edge flashings, Int. J. Roof. Technol. 2 (1990) 65–70.
- [6] H. Jiang, Wind effects on metal edge flashings, Texas Tech University 66 (Issue December) (1995).
- [7] J.R. McDonald, P.P. Sarkar, H. Gupta, Wind-induced loads on metal edge flashings, J. Wind Eng. Ind. Aerod. 72 (1–3) (1997) 367–377, https://doi.org/10.1016/S0167-6105(97)00253-5.
- [8] A. Baskaran, S. Molleti, N. Martins, B. Martín-Pérez, Development of wind load criteria for commercial roof edge metals, J. Architect. Eng. 24 (3) (2018), 04018011, https://doi.org/10.1061/(asce)ae.1943-5568.0000308.
- [9] N.E. Martins, B. Martín-Pérez, A. Baskaran, Application of statistical models to predict roof edge suctions based on wind speed, J. Wind Eng. Ind. Aerod. 150 (2016) 42–53, https://doi.org/10.1016/j.jweia.2016.01.003.
- [10] ASCE, Minimum Design Loads And Associated Criteria For Buildings And Other Structures (Issues 7-22), American Society of Civil Engineers (ASCE), 2022.
- [11] ANSI (American National Standards Institute), Wind Design Standard for Edge Systems Used with Low Slope Roofing Systems, 2017, pp. 1–21. ANSI/SPRI/FM 4435/FS-1
- [12] A.B. Tolera, K. Mostafa, A.G. Chowdhury, I. Zisis, P. Irwin, Study of wind loads on asphalt shingles using full-scale experimentation, J. Wind Eng. Ind. Aerod. 225 (2022), 105005, https://doi.org/10.1016/j.jweia.2022.105005.
- [13] A.B. Tolera, M. Shiao, A. Gan Chowdhury, I. Zisis, P. Irwin, Performance of asphalt shingles under simulated hurricane winds and evaluation of current installation practices, J. Wind Eng. Indust. Aerodynamic 239 (2023), 105456. https://doi.org/10.1016/j.jweia.2023.105456.
- [14] M.T.L. Browne, Z.J. Taylor, S. Li, S. Gamble, A wind load design method for ground-mounted multi-row solar arrays based on a compilation of wind tunnel experiments, J. Wind Eng. Ind. Aerod. 205 (August) (2020), 104294, https://doi.org/10.1016/j.jweia.2020.104294.
- [15] J. Estephan, A. Gan Chowdhury, P. Irwin, A new experimental-numerical approach to estimate peak wind loads on roof-mounted photovoltaic systems by incorporating inflow turbulence and dynamic effects, Eng. Struct. 252 (2022), https://doi.org/10.1016/j.engstruct.2021.113739.
- [16] M. Moravej, A.G. Chowdhury, P. Irwin, I. Zisis, G. Bitsuamlak, Dynamic effects of wind loading on photovoltaic systems, in: 14th International Conference on Wind Engineering (ICWE14), 2015.
- [17] A. Naeiji, F. Raji, I. Zisis, Wind loads on residential scale rooftop photovoltaic panels, J. Wind Eng. Ind. Aerod. 168 (2017) 228–246, https://doi.org/10.1016/J. JWEIA.2017.06.006.
- [18] K.J. Alawode, K.S. Vutukuru, A. Elawady, S.J. Lee, A.G. Chowdhury, G. Lori, Wind-induced vibration and wind-driven rain performance of a full-scale single-skin facade unit with vertical protrusions, J. Architect. Eng. 29 (2) (2023), https://doi.org/10.1061/JAEIED.AEENG-1393.
- [19] K.S. Vutukuru, K.J. Alawode, A. Bakhtiari, A. Elawady, S.J. Lee, A.G. Chowhdury, G. Lori, Full-scale experimental testing to investigate wind-induced vibrations on curtain wall systems, STR-12-1-STR-12-6, Proceedings of International Structural Engineering and Construction 8 (1) (2021), https://doi.org/10.14455/ISEC.2021.8(1).STR-12.
- [20] A.G. Chowdhury, I. Zisis, P. Irwin, G. Bitsuamlak, J.P. Pinelli, B. Hajra, M. Moravej, Large-scale experimentation using the 12-fan wall of wind to assess and mitigate hurricane wind and rain impacts on buildings and infrastructure systems, J. Struct. Eng. 143 (7) (2017) 1–16, https://doi.org/10.1061/(ASCE) ST.1943-541X.0001785.

- [21] A.G. Chowdhury, K.S. Vutukuru, M. Moravej, Full- and large-scale experimentation using the wall of wind to mitigate wind loading and rain impacts on buildings and infrastructure systems, in: Proceedings of the 11th Structural Engineering Convention (SEC18), 2018, https://doi.org/10.1061/(asce)st.1943-541x.0001785.
- [22] H. Irwin, K.R. Cooper, R. Girard, Correction of distortion effects caused by tubing systems in measurements of fluctuating pressures, J. Wind Eng. Ind. Aerod. 5 (1–2) (1979) 93–107
- [23] M.A. Mooneghi, P. Irwin, A.G. Chowdhury, Partial turbulence simulation method for predicting peak wind loads on small structures and building appurtenances, J. Wind Eng. Ind. Aerod. 157 (2016) 47–62, https://doi.org/10.1016/J.JWEIA.2016.08.003.
- [24] M. Moravej, Investigating Scale Effects on Analytical Methods of Predicting Peak Wind Loads on Buildings, [Florida International University, 2018, https://doi.org/10.1017/CBO9781107415324.004.
- [25] P.J. Richards, R.P. Hoxey, Pressures on a cubic building-Part 1: full-scale results, J. Wind Eng. Ind. Aerod. 102 (2012) 72–86, https://doi.org/10.1016/j. iweia.2011.11.004.
- [26] P.J. Richards, R.P. Hoxey, Pressures on a cubic building-Part 2: quasi-steady and other processes, J. Wind Eng. Ind. Aerod. 102 (2012) 87–96, https://doi.org/10.1016/j.jweia.2011.11.003.
- [27] M.L. Levitan, K.C. Mehta, Texas Tech field experiments for wind loads part 1: building and pressure measuring system, J. Wind Eng. Ind. Aerod. 41 (44) (1992) 1565–1576, https://doi.org/10.1016/0167-6105(92)90372-H.
- [28] M.L. Levitan, K.C. Mehta, Texas tech field experiments for wind loads part II: meteorological instrumentation and terrain parameters, J. Wind Eng. Ind. Aerod. 41 (44) (1992) 1577–1588, https://doi.org/10.1016/0167-6105(92)90373-I.
- [29] A.P. Jeary, Establishing non-linear damping characteristics of structures from non-stationary response time-histories, Struct, Eng. 70 (4) (1992) 61–66.
- [30] Y. Tamura, S. Suganuma, Evaluation of amplitude-dependent damping and natural frequency of buildings during strong winds, J. Wind Eng. Ind. Aerod. 59 (2) (1996) 115–130, https://doi.org/10.1016/0167-6105(96)00003-7.
- [31] Z. Wynne, T. Reynolds, D. Bouffard, G. Schladow, D. Wain, A novel technique for experimental modal analysis of barotropic seiches for assessing lake energetics, Environ. Fluid Mech. 19 (6) (2019) 1527–1556, https://doi.org/10.1007/s10652-019-09677-x.
- [32] D. Banks, T.K. Guha, Y.J. Fewless, A hybrid method of generating realistic full-scale time series of wind loads from large-scale wind tunnel studies: application to solar arrays, in: Proceedings of the 14th International Conference on Wind Engineering, 2015.
- [33] A. Baskaran, S. Molleti, T. Mallinger, B. Martín-Pérez, In-situ measurement of wind performance of roof edge systems, 32nd RCI International Convention and Trade Show (2017) 89–96.
- [34] ASCE, Minimum design loads for buildings and other structures, in: ASCE Standard, American Society of Civil Engineers, 2010 (ASCE).
- [35] ASCE, Minimum Design Loads and Associated Criteria for Buildings and Other Structures, American Society of Civil Engineers, 2017 (ASCE).
- [36] Z. Azzi, F. Habte, K.S. Vutukuru, A. Gan Chowdhury, M. Moravej, Effects of roof geometric details on aerodynamic performance of standing seam metal roofs, Eng. Struct. 225 (2020), 111303, https://doi.org/10.1016/j.engstruct.2020.111303.
- [37] C. Blessing, A.G. Chowdhury, J. Lin, P. Huang, Full-scale validation of vortex suppression techniques for mitigation of roof uplift, Eng. Struct. 31 (12) (2009) 2936–2946, https://doi.org/10.1016/j.engstruct.2009.07.021.
- [38] A.P. Robertson, Effect of eaves detail on wind pressures over an industrial building, J. Wind Eng. Ind. Aerod. 38 (2–3) (1991) 325–333, https://doi.org/10.1016/0167-6105(91)90051-W.